

Influence of Oxide Growth and Metal Creep on Strain Development in the Steam-Side Oxide in Boiler Tubes

Adrian S. Sabau · Ian G. Wright

Received: 8 September 2009 / Revised: 7 December 2009 / Published online: 10 January 2010
© Springer Science+Business Media, LLC 2010

Abstract This effort is concerned with developing a quantitative description of the exfoliation behavior of oxide scales grown inside steam tubes in a pressure boiler. Consideration of the development of stress/strain in growing oxides has included expansion mismatch-induced strains during thermal cycling as well as inelastic mechanical effects from oxide/alloy creep phenomena and volume change from oxide growth. The magnitude of the parameters used has been closely matched to actual boiler operating practice. The creep model used was validated against published data. Representation of oxide growth-induced strain was found to be a difficult challenge because the processes involved are not fully understood. In addition to the traditional uniaxial (radial) and dilatational models, ‘lateral’ growth models are discussed in the context of experimentally-derived criteria, such as the level of elastic strains involved in oxide exfoliation. It was found that strain variation in the oxide cannot be neglected.

Keywords Oxide growth-induced stresses · Creep · Growth-induced strain · Modelling · Boiler tube

Introduction

This study was aimed at developing a mathematical model capable of providing guidance on the influence of the key variables in the processes that result in the failure and spallation/exfoliation of oxide scales formed on the steam-touched surfaces in power generation boilers. The model is based on available constitutive equations of the numerous contributing processes with the intent that knowledge of

A. S. Sabau (✉) · I. G. Wright
Materials Science and Technology Division, Oak Ridge National Laboratory,
Oak Ridge, TN 37831, USA
e-mail: sabaua@ornl.gov

specific changes among boiler configuration and operating conditions, as well as differences in alloy properties and oxidation behavior, can be incorporated to allow the model to use actual variables, rather than to employ a data-fitting approach [1]. As a result, the model is modular in construction, and provides the facility for revising each module independently as improved understanding of a given area is developed. This paper is concerned with the considerations involved in establishing a mechanistic description of the contributions to stress–strain development in oxide layers from the volume change associated with oxide growth, and relaxation due to creep that take place during boiler operation. Finally, the inelastic effects resulting from creep and from volume change due to oxide growth on the processes leading to the spallation of oxides grown on alloy T22 (Fe-2.25Cr-1Mo, wt%) are evaluated.

Most considerations of the development of stresses in oxide scales have emphasized those derived from differences in coefficients of thermal expansion and from phase transformations [1], while stresses arising from the volume change associated with oxide growth have been considered initially to be substantially relieved at high temperature (for growth on a flat, infinitely-long specimen) and therefore to be of lower importance [2]. In a recent review of possible mechanisms for oxide growth-induced strains, Panicaud et al. [3] concluded that partially as a result of this focus, as well as the dependence on geometrical considerations and difficulties in measuring such stresses and strains, the nature and expression of the stresses associated with oxide growth have not received the same level of attention and are less well understood. These authors also initiated measurements of oxide growth-induced (OGI) stresses for scales containing Fe_3O_4 and Fe_2O_3 , although for relatively thin oxides (oxidation times up to 20 h) [4, 5].

Various approaches for rationalizing the extent of OIG stresses have been proposed over the years [6]. Rhines and Wolf [7] suggested that no lateral strains are created when the oxide grows normal to the metal–oxide interface in any of the following situations: (a) at the oxide–gas interface via outward diffusion of metal ions, (b) at the oxide/alloy interface via inward diffusion of oxygen ions or, (c) at grain boundaries lying parallel to the oxide/alloy interface, since rigid outward displacement of the oxide would accommodate such strain, resulting in the oxide being stress-free. As oxides thicken, the way in which their morphologies evolve is strongly influenced by the need to accommodate the changes in volume of the oxide and metal. For an oxide predominantly growing by outward cation diffusion, for example, a columnar-grained structure normal to the metal–oxide interface is often developed. Usually, the oxide grain diameter is smaller than the length, and this has been attributed to movement of cations from the oxide (columnar) grain boundaries to the oxide–gas interface due to diffusional creep caused by compressive (lateral) stresses in the oxide [8]. This augmented flux of outward-flowing cations also contributes to the grain growth observed in growing oxides (see, for instance, Tolpygo et al. [9]), such that the grain diameter increases with increasing distance from the alloy surface. Expectations that the location of oxide growth will be determined by terminal local activities in the oxide (i.e. either interface) notwithstanding, and following Rhines and Wolf's arguments [7], growth of oxide along oxide grain boundaries aligned normal to the metal–oxide interface has been proposed as a basis for

relating the development of lateral stresses to oxide growth [6, 8, 10]. Stott [6] pointed out that an additional consequence of oxide formation in this location is sliding at the oxide–metal interface, which has consequences for the development of wavy interfaces and convoluted oxide scale morphologies.

On the basis of oxide growth occurring on oxide grain boundaries normal to the metal–oxide interface, Hsueh and Evans [11] suggested that growth-induced deformations should be taken into account through eigenstrains ($\varepsilon_{r,ox}$, $\varepsilon_{\theta,ox}$, $\varepsilon_{z,ox}$) given by the theoretical volumetric ratio between oxide and metal ($\Phi - 1$), where Φ is the Pilling–Bedworth ratio [12]. However, the eigenstrain based on ($\Phi - 1$) was shown to result in the prediction of unrealistically high stresses [13, 14]. Bernstein [13] used considerations of the effects of physical constraint resulting in preferred directions of oxide growth (mostly normal to the alloy surface) to argue that the effective OGI strain is a fraction of the theoretical value, i.e. $\omega (\Phi^{1/3} - 1)$. Evans and Cannon [15] also proposed a model for stress-driven oxide-growth, which was extended by Limarga et al. [16] to include the diffusion fluxes of anions and cations along oxide grain boundaries and the metal/oxide interface. Clarke also considered sources of OGI strain where oxides grow by short circuit diffusion along grain boundaries, with inward and outward flux of ions and oxide formation mainly at interfaces, but also some growth on grain boundaries. They concluded that the mode and rate of growth of the oxide influence the OGI strain and its location [10, 17]. Recently, Panicaud et al. [18, 19] revisited these ideas, and presented asymptotic solutions for the differential equations for diffusion and creep relaxation phenomena in oxides. Experimental data for the stress evolution during the initial oxide growth of scales containing Fe_3O_4 and Fe_2O_3 were used to estimate a model parameter for the OIG over a flat plate [19].

The approach of specifying oxide-growth eigenstrains is an ongoing activity in the research community and some recent studies, such as that by Steiner et al. [2], have continued to use the eigenstrain formulation based on the theoretical volumetric ratio between oxide and metal. Oh et al. [20] solved the combined system of equations for (a) the generalized Hooke's law in an unknown current state, (b) the mole balance for the metal between the consumed metal and that in the oxide formed, and (c) the diffusion of species in the oxide. In this approach, the combination of the diffusion and mole balance equations allows the widely-used assumption of specifying a priori eigenstrain due to oxide growth to be discarded. Rather, the *equivalent* eigenstrain can be obtained as a function of oxidation time and, for small oxide thicknesses, this was shown to be a fraction of ($\Phi - 1$), in good agreement with the assumption made by Bernstein [13]. Oh et al. [20] indicated, however, that an oxidation eigenstrain of ($\Phi - 1$) is appropriate only for the final stages of oxidation, i.e., when the metal has oxidized almost entirely.

While there have been few reports of the values of actual OGI stresses, Tolpygo et al. [9] measured the growth stress and strains for $\alpha\text{-Al}_2\text{O}_3$ scales by using plates of FeCrAlY of different thicknesses to take into account thermal expansion and creep phenomena. They found that significant growth strains (as high as 0.04) could be developed.

In this study an eigenstrain approach was employed to account for OGI stresses, while stress relaxation was considered to occur by creep in the metal *and* oxide.

In the absence of any published work that explicitly considers the diffusion of species involved in the growth of the oxides on the stress resulting from the volume of oxide grown, in this study Bernstein's correction factor (ω) was adopted as an empirical factor. Constitutive equations were formulated for the solution of the stress–strain relationships for a plane-strain approximation in axi-symmetrical geometry. Several cases were evaluated for each formulation of oxidation strains, and the resulting model for OGI stress (in the absence of creep phenomena) was validated against published data for a metal tube without an oxide scale [2]. For creep, a review of constitutive equations for the creep rate for metal and oxide layers as a function of stress and temperature resulted in the use of a Norton's law [21, 22] for the creep rate for both metal and oxide layers considered. The results for the strains, von Mises stress, and creep strains were used to evaluate various models for the calculating oxidation strains.

Constitutive Equations

A previously-developed model for stress evolution during oxide growth [23] was extended to include the eigenstrain formulation for oxide growth and creep phenomena. The modifications consisted of the addition of terms due to oxidation strains, $\varepsilon_{r,ox}$, $\varepsilon_{\theta,ox}$, $\varepsilon_{z,ox}$ and creep strains, $\varepsilon_{r,cr}$, $\varepsilon_{\theta,cr}$, $\varepsilon_{z,cr}$. The oxide growth strains were considered to be constant in the oxide. The oxide thickness, $d_{ox(k)}$, at a given time, t_k , is given by:

$$d_{ox(k)}^2 = d_{ox(k-1)}^2 + d(d_{ox}^2) \quad (1)$$

where $d(d_{ox}^2) = 2 \Delta t k_p [T_{gr}(t_k)]$ denotes the usual increment for the scale growth in a time interval, $\Delta t = t_k - t_{k-1}$, at a temperature, $T_{gr}(t_k)$, according to the specific temperatures for the full load and partial load of the boiler cycle for the parabolic oxidation relationship. $k_p(T) = A e^{-Q/RT}$ indicates that the parabolic rate constant (k_p) corresponds to the prevailing oxide growth temperature, A is the Arrhenius constant; Q the activation energy for the rate-controlling process; R is the Universal Gas Constant; and T is the oxide growth temperature, T_{gr} . The oxidation parameters used for alloy T22 were: $A = 1.51 \times 10^{14} \mu\text{m}^2/\text{h}$ and $Q = 223 \text{ kJ/mole}$ [1, 23].

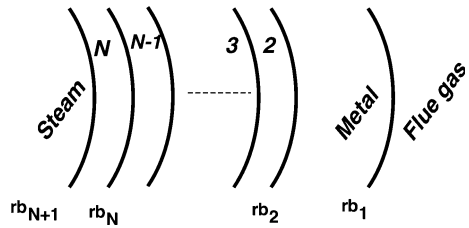
For a given material specified by the index i , the free thermal strain (ε_{th}) resulting from a temperature variation (say, T_1 to T_2) is defined as:

$$\varepsilon_{th,i}(T_1, T_2) = \int_{T_1}^{T_2} \alpha_i(T) dT \quad (2)$$

where α is the coefficient of thermal expansion. The strain–stress equations for a plane-strain approximation in axi-symmetrical geometry (Fig. 1) are:

$$\varepsilon_{r,ij} - \varepsilon_{r,ox} - \varepsilon_{r,cr} = \frac{\sigma_{r,ij} - \nu_i^* \sigma_{\theta,ij}}{E_i^*} + (1 + \nu_i) \varepsilon_{th,i}(T_R, T_{ij}) + \nu_i (\varepsilon_{z,ox} + \varepsilon_{z,cr} - \varepsilon_o) \quad (3)$$

Fig. 1 Schematic representation of the tube configuration with oxide growth on the steam side



$$\varepsilon_{\theta,ij} - \varepsilon_{\theta,ox} - \varepsilon_{\theta,cr} = \frac{\sigma_{\theta,ij} - v_i^* \sigma_{r,ij}}{E_i^*} + (1 + v_i) \varepsilon_{th,i}(T_R, T_{ij}) + v_i (\varepsilon_{z,ox} + \varepsilon_{z,cr} - \varepsilon_o) \tag{4}$$

where $\varepsilon_{r,ij}$ is the strain in the radial direction; $\varepsilon_{\theta,ij}$ is the total hoop strain; ε_o is the constant axial strain, i.e., $\varepsilon_z = \varepsilon_o = const.$; $\varepsilon_{r,ox}$, $\varepsilon_{\theta,ox}$, $\varepsilon_{z,ox}$ are the OGI strains in the radial, hoop, and axial directions, respectively; $\varepsilon_{r,cr}$, $\varepsilon_{\theta,cr}$, $\varepsilon_{z,cr}$ are the creep strains in the radial, hoop, and axial directions, respectively; σ_r is the total radial stress; and σ_{θ} is the total hoop stress.

Each i -th layer was discretized with M_i number of grid points. Thus, the displacement in the radial direction is given by $u_{ij} = r_j \varepsilon_{\theta,ij}$. For the plane-strain assumption, the effective Young’s modulus (E_i^*) and Poisson’s ratio (v_i^*) are given by:

$$E_i^* = E / (1 - v_i^2) \tag{5}$$

and

$$v_i^* = v_i / (1 - v_i) \tag{6}$$

Over the range of temperatures considered (400–600 °C), the Young’s modulus exhibits a small variation (2–3% for the oxide layer [14]), while variation in Poisson’s ratio is neglected [14], so that for each layer in Fig. 1 both parameters were considered to be constant. Further details of the integration of these equations are given in Appendix 1.

Computational Cycle

For the sake of simplicity, the computation of the oxide thickness was decoupled from that of the stress analysis. First, the oxide thickness (d_{ox}) grown during the boiler load cycle was found using a few iterative steps [23] that accounted for fact that oxide growth occurred in a temperature gradient, with the value of T_{gr} increasing with oxide thickness. Then, during each boiler cycle (full or partial load), the state of stress and strain was computed using several iterations, accounting for the effect of the level of creep strains which are not known a priori. The convergence criterion depended on the convergence of von Mises stresses, based on the L_2 -norm of the von Mises strain increment between the stress at the previous stress iteration ($k - 1$) and the stress at the current iteration (k) over the value of von Mises stresses, as:

Table 1 Computational cycle when creep effects are included

Start load cycle, m
(1) $T_{gr} = T_{st}$
(2) Oxide thickness, $d(T_{gr})$
(3) dimensions, r_b
(4) T distribution
(5) Thermal expansion
(6) Start stress loop, k
(6.1) Creep rate, $\dot{\epsilon}_{cr}(\sigma_{eq}^{k-1}, T)$
(6.2) Creep strain, $\epsilon_{k,cr}(t + \Delta t) = \epsilon_{k,cr}(t) + \Delta t \dot{\epsilon}_{cr}$
(6.3) New solution: σ^k, ϵ^k
(6.4) Von Mises stress, σ_{eq}^k
(6.5) Error = $ \sigma_{eq}^{k-1,k} _2$
(6.6) End stress loop if error $< 10^{-4}$
End load cycle after a given time period

$$|\sigma_{eq}^{k-1,k}|_2 = \sqrt{\sum_{i=1}^M \left(1 - \sigma_{eq}^{k-1} / \sigma_{eq}^k\right)^2} / \sqrt{M} \quad (7)$$

The stress iterations consisted of the following steps, which are also summarized in Table 1:

- Obtain the creep rate based on the previous von Mises stress;
- Obtain the creep strain for the current time interval using the new creep rate;
- Obtain a new solution for the stress and strains using the new creep strains;
- Obtain von Mises stresses based on the newly-computed stresses
- Evaluate the $|\cdot|_2$ error based on the ratio between the previous and new von Mises stresses.

The iterations ended when the $|\cdot|_2$ error was smaller than the acceptable error (taken as 10^{-4}).

Creep Properties

This study considers viscoelastic creep in the steady-state creep domain only, since normally the components are retired before the tertiary creep domain would be attained under normal boiler operating conditions. The primary creep regime was not considered since (a) it extends for a very limited time, e.g., from the data presented in Fig. 1 [22], the duration of the primary creep domain was estimated to be less than 2,000 h for a 2.25Cr1Mo steel at 550 °C and 40 MPa, and (b) the creep strain attained in this regime is very small. If available, data for the creep strain as a function of temperature and stress, similar to those presented in [22] for the primary, steady-state, and tertiary domains, can be used easily into our approach instead of the steady-state creep strain rate function used in this paper. For the steady-state creep domain, the material undergoes creep deformation at a rate given by the

secondary creep rate, or minimum creep rate. Creep properties usually are specified as a function of von Mises stress and temperature, $\dot{\epsilon}_{cr}(\sigma_{eq}, T) = f(\sigma_{eq}) g(T)$ [24]. For Norton's law, the stress dependence is given as:

$$f(\sigma_{eq}) = A_{cr}(\sigma_{eq})^n \quad (8)$$

where A_{cr} and n are model parameters determined from experimental data. The temperature effect usually is considered through an Arrhenius law, involving a creep activation energy, Q_{cr} , as:

$$g(T) = \exp\left(-\frac{Q_{cr}}{RT}\right) \quad (9)$$

According to the deformation map proposed by Frost and Ashby [24], the creep mechanism depends on the stress (σ_{eq}) and temperature (T). Without including the creep effects, the computational results for the von Mises stresses indicated that the σ_{eq}/G varies between 2.08×10^{-4} and 5.89×10^{-4} for the full regime, and 1.09×10^{-4} and 3.76×10^{-4} for the partial regime, respectively. The temperature results indicated that T varies between 580 and 600 °C for the full regime, and 464 and 466 °C for the partial regime, respectively. The melting point, T_m , for the alloy considered (T22) is approximately 1538 °C [25] and T/T_m varies between 0.4 and 0.48. According to the deformation maps proposed by Frost and Ashby [24], at these temperatures and stresses the alloy is expected to exhibit a combination of low-temperature creep and power-law creep.

A literature review was conducted to identify the creep properties for T22. Cane [25] provides experimental data for creep of T22 but does not specify the activation energy, Q_{cr} , or the stress exponent. Activation creep energies of 400 kJ/mol (for low-temperature creep) and 251 kJ/mol (for power-law creep) were obtained from the literature [24, 26, 27] and were used to identify the parameters for the creep rate given by the Norton's law. The data presented by Cane [25] indicated that at 550 °C and $\Sigma = 85$ MPa, and at 575 °C and $\Sigma = 59$ MPa, $\dot{\epsilon}_{cr}$ was $2E-6$ and $1.765E-6$ (1/h), respectively. These creep parameters for T22 are shown in Table 2.

The oxide scale formed on alloy T22 in steam typically consists of magnetite (Fe_3O_4) and Fe–Cr spinel layers [30]. The melting temperature for magnetite is 1538 °C [13] which is very close to that of T22. Thus, for the boiler operating parameters considered, creep phenomena in magnetite cannot be neglected.

Table 2 Creep parameters

Material	Q_{cr}/R (1/K)	A_{cr} (1/h)	n	References
T22	48,100	8.27E+09	5.06	This study based on Qcr: Shi and Endo [26] Creep data: Cane [25]
T22	30,190	7191.18	3.30	This study based on Qcr: van der Burg et al. [27] Creep data: Cane [25]
T22	41,000	4.3E+7	4.57	Mayer and Manolescu [28]
Fe_3O_4	3.18E+4	2.29E+07	3	Crouch and Robertson [29]

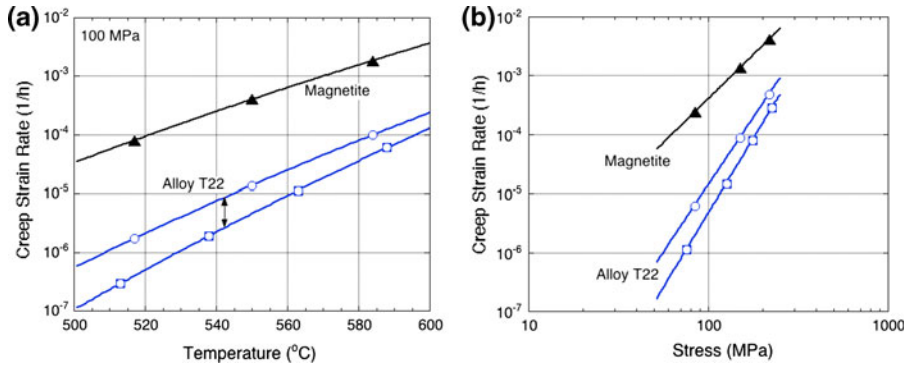


Fig. 2 Dependence of creep rate of alloy T22 alloy and magnetite on **a** temperature (at 100 MPa), and **b** stress (at 550 °C), after Crouch and Robertson [29]

The creep properties reported for Fe₃O₄ by Crouch and Robertson [29] are shown in Table 2. In the absence of available data, and based on the fact that the Fe–Cr spinel is iso-structural with magnetite, the creep properties of the spinel were taken to be the same as those of magnetite. Also, the tension/compression anisotropy of the oxides is not considered here. In this study, the creep rate for alloy T22 was considered to be that given in the first line shown in Table 2. The temperature dependence of the creep rate, at a constant stress of 100 MPa, and the stress dependence of the creep rate at a constant temperature of 550 °C, are shown in Fig. 2.

Validation of the Solution Algorithm for the Oxide Growth-Induced Stress Module

First, the OGI stress model was tested for the same configuration as that of Steiner et al. [2]. The results for this oxidation-strain case were obtained with $\Phi = 2$ and $\omega = 1$, i.e., $\epsilon_{r,ox} = \Phi - 1$, $\epsilon_{\theta,ox} = 0$, and $\epsilon_{z,ox} = 0$. The metal thickness was 990 μm , and the thickness of the oxide (which was grown on the outer surface of a cylinder with ID = 6 mm) was 11 μm . The results presented in Table 3 are in very good agreement to those of Steiner et al. [2]. Since this study focuses on an oxide scale that grows on the *internal* surface of a

Table 3 Hoop strain and stresses due to oxide-induced stresses, radial option, in the metal and oxide for an 11 μm thick oxide grown on the outer surface of a cylinder

Location	1,000 ϵ_{θ}^s	σ_{θ} (MPa)	σ_r (MPa)	σ_z (MPa)
Metal surface	-0.0189	-3.32	0	-0.964
Metal (M–O interface)	-0.0130	-2.60	-0.722	-0.964
Oxide (M–O interface)	-0.0130	-2.86	-0.722	-1.00
Oxide (mid plane)	1.35	265	-0.543	76.7
Oxide surface	2.71	532	0	154

Table 4 Hoop strain and stresses due to oxide-induced stresses, radial option, in the metal and oxide for a 10.4 μm thick oxide grown on the inner surface of a cylinder

Location	1,000 ϵ_{θ}^s	σ_{θ} (MPa)	σ_r (MPa)	σ_z (MPa)
Metal surface	0.0172	3.03	0	0.879
Metal (M–O interface)	0.0267	4.19	−1.16	0.879
Oxide (M–O interface)	0.0267	4.77	−1.16	1.01
Oxide (mid plane)	−1.71	−336	−0.879	−97.8
Oxide surface	−3.45	−678	0	−197

Table 5 Hoop strain and stresses due to oxide-induced stresses, dilatational option $\epsilon_{r,ox} = \epsilon_{\theta,ox} = \epsilon_{z,ox} = \Phi^{1/3} - 1$, in the metal and oxide for an 11 μm thick oxide grown on the outer surface of a cylinder

Location	1,000 ϵ_{θ}^s	σ_{θ} (MPa)	σ_r (MPa)	σ_z (MPa)
Metal surface	4.65	817	0	817
Metal (M–O interface)	3.21	640	178	817
Oxide (M–O interface)	−332	−6.52E+04	178	−6.50E+04
Oxide (mid plane)	−331	−6.51E+04	88.6	−6.50E+04
Oxide surface	−331	−6.50E+04	0	−6.50E+04

cylinder, a test case was run for a 10.4 μm thick oxide grown on the outer and inner surfaces of a cylinder with ID = 6 mm. For the inner oxide scale, the results are presented in Table 4, which indicates that the strain and stresses have approximately the same absolute value, while the axial and hoop strain changes from compression to tension in the metal.

Another assumption commonly used for OGI stresses is that of dilational oxide growth. The results of calculations using the dilational assumption of OGI stresses ($\epsilon_{r,ox} = \epsilon_{\theta,ox} = \epsilon_{z,ox} = \Phi^{1/3} - 1$) are presented in Table 5. Note that the results for the oxide hoop strain, hoop and axial stresses are extremely high, indicating that this assumption is unrealistic.

Validation of the Solution Algorithm for the Creep Module

The creep model was tested for a similar configuration to those of Brown [31] and Zarrabi and Ng [32]. The growth of an oxide scale was not considered in the simulations that were conducted for the model validation in order to match the approach used by Zarrabi and Ng [30]. The creep strain rate of was $\dot{\epsilon}_{cr}(\sigma_{eq}) = 6.103 \times 10^{-33} (\sigma_{eq})^{11.98} \left[1 + \exp\left(t - 10^{(367.79 - \sigma_{eq})/57.774}\right) \right]$. The Young’s modulus was 1.542×10^5 MPa, and the outside and inside diameters of the tube were considered to be 40 and 33.4 mm, respectively. Although there are some differences in the assumptions and loading of the tube between this study and that of Zarrabi and Ng [32] (as indicated in Table 6), a comparison between the results obtained in this study can be used to assess qualitatively the accuracy of the methodology employed in this study.

Table 6 Problem assumptions and loading conditions for validation simulations

Location	Zarrabi and Ng [32]	This study
Assumptions	symmetry at $z = 0$, $\sigma_z = \text{const.}$ at $z = 50$ mm	Plain-strain
Solution method	2D finite element method	Semi-analytical integral formulation
σ_r (MPa) inside	28.77	28.77
σ_z (MPa)	66.26	$\int_{rb_{N+1}}^{rb_1} \sigma_z r dr = 33.13(rb_1^2 - rb_{N+1}^2)$

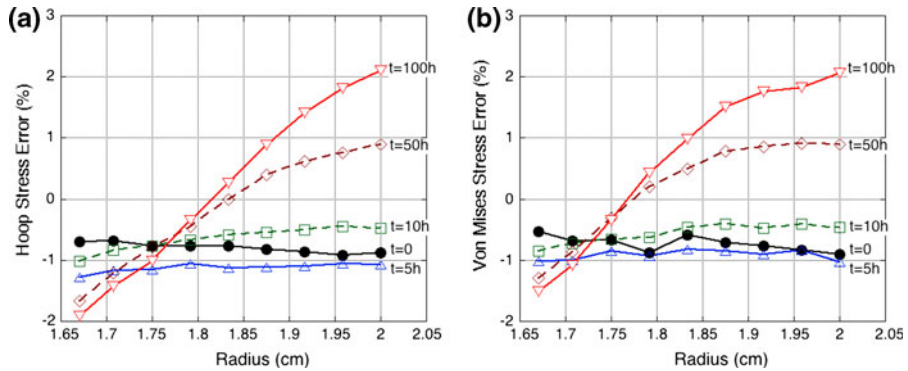


Fig. 3 Radial distribution of the relative error ($100 \times (\sigma - \sigma_{ZN})/\sigma_{ZN}$) in calculating **a** the hoop stress; and **b** the Von Mises stress, with respect to the stress values from Zarrabi and Ng [32], as a function of time since the onset of creep

In Fig. 3 results are presented for the radial distribution of the relative error of the hoop stress ($100 \times (\sigma - \sigma_{ZN})/\sigma_{ZN}$) and Von Mises stress with respect to the stress values that were obtained by Zarrabi and Ng [32]. Results are shown at various times following the onset of creep. At the onset of simulations (i.e., $t = 0$) the relative error was 1%, indicating a systematic error between this model and that by Zarrabi and Ng [32]. The relative stress error varied between -0.5 and -1% for times of 5 and 10 h, and stayed below 2% at times of 50 and 100 h in spite of the dramatic change in the stress distribution due to creep relaxation [32]. Overall, these results show that the stresses obtained in this study were in very good agreement with those reported by Zarrabi and Ng [32].

Boiler Operation

The parameters for boiler operation were reviewed based on data published from experimental and computational studies on the industrial practice of boiler operation, such as heat flux variation between the full load and partial load regimes. The boiler tubes of interest were considered to have an outside diameter of 50 mm and a wall thickness of 11 mm. The heat flux at partial load was taken to be a given fraction (q_p) of that at full load. A review of the open literature indicated that

Table 7 Data on boiler operation

Component	Flue gas temperature (°C)	T_M (°C)	T_{st} (°C)	Heat Flux (W/m ²)	Study type	References	Comments
Superheater	1090	495–540	437	20–150	Comp.	Pronobis et al. [33]	Circumferential and radial
Reheater	–	525–595	–	–	Exp-comp	Xu et al. [34]	Measured outside wall at the ‘final reheater outlet tubes’
Superheater	900–980		420–430		Exp-comp	Benyo et al. [35]	
Superheater	820–1020	520–570 (full) 510–550 (partial)	380		Exp	Gonzales et al. [36]	Full/partial load load

the measured metal temperature (midwall) varies only slightly between partial and full load (Table 7).

Partial load was assumed to be achieved by decreasing the flows of combustion gas and steam (subcritical steam boiler). Although in practice at partial load the combustion gas temperature (T_g) would be essentially constant while the heat transfer coefficients (HTCs) would vary according to the flow conditions, in the absence of detailed information about actual flow rate variations, for this approach it was considered that the HTCs do not change with the combustion gas and steam flow rates from full to partial load. Thus, it was necessary to estimate T_g at partial load in order to attain the imposed heat flux. The boiler operating conditions assumed are shown in Table 8.

For the values of the boiler operating parameters shown in Table 8, the heat flux at full load was calculated to be 50 W/m², and T_g at partial load was estimated to be 810 °C. The value obtained for heat flux was close to the 45 kW/m² used by Mayer and Manolescu [28]. The evolution of the temperatures of the metal outer surface, metal–oxide interface, and oxide surface as a function of oxide growth are shown in Fig. 4. It was found that at full load the metal temperature on the outer (inner) side of the tube wall increased from 586 (560) °C for a new tube to approximately 595

Table 8 Assumed boiler operating conditions

Load	Duration (h)	q_f	T_g (°C)	T_{st} (°C)	P_g (bar)	P_{st} (bar)
Full	14	1	1,100	530	2	170
Partial	8	0.5	845	525	1	100
Shutdown	25	N/A	25	25	1	1

$$\Delta t_{F-P} = \Delta t_{P-F} = 1 \text{ h}, \Delta t_{F-RT} = 3 \text{ h}; \Delta t_{RT-F} = 6 \text{ h}$$

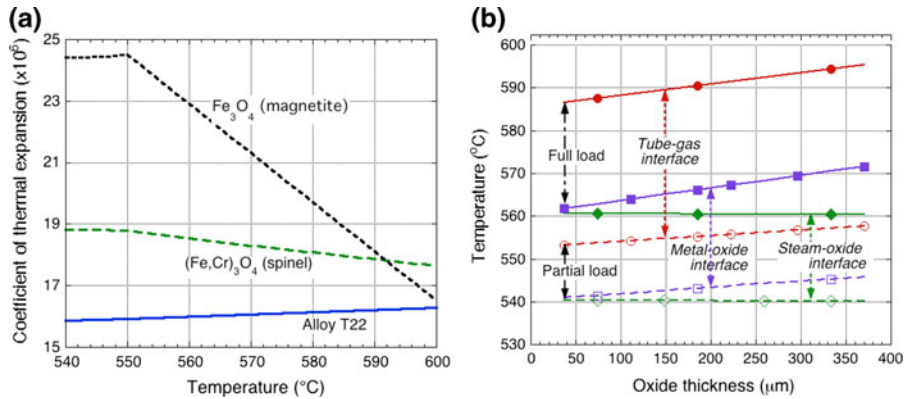


Fig. 4 **a** Temperature dependence of the coefficients of thermal expansion for alloy T22 and the oxides considered (after Armit et al. [37]), and **b** evolution of temperature with increasing oxide thickness at the tube–combustion gas interface, metal–oxide interface, and steam–oxide interface at full load and partial load conditions

(570) $^{\circ}\text{C}$ at a steam-side oxide thickness of 360 μm , the maximum metal temperature being very close to the value (596 $^{\circ}\text{C}$) measured by Gonzales et al. [36]. At partial load, the corresponding temperatures were 552 (540) $^{\circ}\text{C}$ for a new tube and 558 (550 $^{\circ}\text{C}$) for a tube with a 360 μm -thick oxide. The boiler operating campaign was considered to last approximately 5.5 years with shutdown events every 11 months. The parameters related to a shutdown event also are indicated in Table 8.

Numerical Simulation Results

The temperature dependence assumed for the coefficient of thermal expansion of alloy T22, magnetite, and the Fe–Cr spinel were those of Armit et al. [37], shown in Fig. 4a for the range of temperatures experienced by the tube. Figure 4b illustrates the calculated evolution of temperature with increasing oxide thickness at the tube–combustion gas interface, metal–oxide interface, and steam–oxide interface at full load and partial load conditions. Note that the oxide thickness in the abscissae of these plots is the total scale thickness (magnetite + spinel); the relative thicknesses of the magnetite and spinel layers are similar, but the spinel layer is approximately 10% thicker because its growth temperature was assumed to be that of the alloy–oxide interface, which is higher than that of the oxide–steam interface at which the magnetite was assumed to grow.

In the following figures, numerical simulation results are presented for several cases in order to investigate the effect of OGI strain and creep phenomena on the evolution of the state of strain and stress. The results for the elastic hoop strain, $\varepsilon_{\theta,el} = \varepsilon_{\theta} - \varepsilon_{\theta,ox} - \varepsilon_{\theta,cr} - \varepsilon_{th}$, are shown first, as this is the main variable considered in most studies of criteria for oxide spallation. Unless otherwise specified, the results shown are for the *average* strain through the thickness of the

Table 9 Assumption on oxide-growth-induced strains

Notation	Assumption	Comments/references
DIL_{ω}	$\varepsilon_{r,ox} = \varepsilon_{\theta,ox} = \varepsilon_{z,ox} = \omega (\Phi^{1/3} - 1)$	$\omega = 1$ (Pilling and Bedworth [12]) $\omega < 1$ (Bernstein [13])
RAD_{ω}	$\varepsilon_{r,ox} = \omega (\Phi - 1), \varepsilon_{\theta,ox} = \varepsilon_{z,ox} = 0$	$\omega = 1$ (Hsueh and Evans [11]) $\omega < 1$ This study
$LAT_B RAD_{\omega}$	$\dot{\varepsilon}_{\theta,ox} = \dot{\varepsilon}_{z,ox} = \dot{d}/B, \varepsilon_{r,ox} = \omega (\Phi - 1) - \varepsilon_{\theta,ox} - \varepsilon_{z,ox}$	This study

oxide layer, since most studies of oxide strains use approximations that are meant to evaluate the average strain in the oxide. Several simulations were conducted to assess the effects of various OGI strain parameters, and in others boiler shut-down events were included in the schedule as a means of investigating the effect of temperature (and pressure) drop in the boiler on the evolution of strain, stress, and/or energy levels in the oxide scale. Finally, the evolution of the hoop strain that generates stress ($\varepsilon_{\theta}^s = (\sigma_{\theta} - \nu^* \sigma_r)/E^*$), which is traditionally used to predict the possibility of spallation [23], was investigated during shut-down events after different time intervals.

Effect of Creep and Oxide Growth-Induced Strains

Several OGI strain models were considered in this study (Table 9). The traditional dilatational model is referred to as DIL_{ω} , where $\omega < 1$ is an empirical factor introduced by Bernstein [6] in order to reduce the unrealistically high OGI stresses that were obtained with $\omega = 1$. The traditional uniaxial model, used by Hsueh and Evans [11] and Steiner et al. [2], is referred to as RAD_{ω} . By analogy to the DIL_{ω} model, the empirical factor ω also was considered for the RAD_{ω} cases. The last series of cases considered represented an attempt to include in the eigenstrain formulation the latest developments in ‘lateral’ OGI strain models, which were developed based on microstructural considerations. Essentially, the ‘lateral’ OGI strain models were intended to relax the uni-axial RAD models by including OGI strains in other directions. The models for OGI stresses in the ‘lateral’ direction can, in general, be represented as [7, 9, 10]:

$$\dot{\varepsilon}_{ox} = \dot{d}/B \tag{10}$$

i.e.

$$\dot{\varepsilon}_{\theta,ox} = \dot{d}/B, \varepsilon_{z,ox} = \varepsilon_{\theta,ox}, \varepsilon_{r,ox} = 0 \tag{11}$$

where B is a proportionality constant with units of length. In this study it was considered necessary to broaden this approach to include the OGI strains in the radial/normal direction.

One of the main obstacles in integrating the lateral OGI strain models into stress–strain analyses is the lack of data for the OGI radial strain ($\varepsilon_{r,ox}$) in all the lateral OGI strain models. In an attempt to include the lateral OGI strains, $\varepsilon_{r,ox}$ was considered to be obtained such that the total volumetric OGI strain is constrained by

Table 10 Simulation cases considered

Case	OGI strain model	Metal creep	Oxide creep
NG–NC	No	No	No
NG	No	Yes	Yes
D–NOC	DIL _{0.1}	Yes	No
D	DIL _{0.1}	Yes	Yes
R1	RAD ₁	Yes	Yes
R2	RAD _{0.1}	Yes	Yes
RL1	LAT _{20,000} RAD _{0.1}	Yes	Yes
RL2	LAT _{100,000} RAD _{0.1}	Yes	Yes
RL3	LAT _{500,000} RAD _{0.1}	Yes	Yes

$\omega(\Phi - 1)$ [2], using a factor ω based on considerations similar to those by Bernstein [13]. These cases are referred to as $LAT_B RAD_\omega$. To date, there is no methodology to choose the OGI strain parameters such as ω (and B). The possibility that the OGI strain parameters may not be constant within the oxide layers also must be considered. As shown by Oh et al. [20] for the dilatational formulation, it is expected that OGI strain parameters vary with oxide thickness. It is thus difficult to obtain OGI strain parameters based solely on experimental results, so that there is a need to explore methodologies based on experimental results and theoretical diffusion models. Based on the review of constitutive models presented above, several OGI strain models were considered in this study (Table 9). These cases were based on the three main OGI strain models and, as shown in Table 10, included creep phenomena.

Case NG–NC: OGI Strain Phenomena and Creep Are Not Considered

Figure 5a plots the evolution of elastic hoop strain in the oxide layers (based on thermal expansion considerations alone) as a function of oxide thickness grown over a period of four years of boiler operation (using the load cycle shown in Table 8, with no shut downs). Whereas under full load conditions the strains in the magnetite and spinel layers are small, tensile and of similar levels, they do not change significantly with increasing oxide thickness. However, under partial load conditions the strains in both oxides are lower and decrease with increasing oxide thickness. At partial load the strain in the magnetite layer at 50 μm thickness is approximately 77% of that at full load, and decreases further to 55% at a scale thickness of 350 μm . The corresponding values for the spinel layer are approximately 26 and 21%, respectively.

The evolution of strain during transition from full load to partial load is shown in Fig. 5b, which indicates that the strain decreases in essentially a linear fashion as a function of oxide surface temperature in both the magnetite and spinel layers. As noted from Fig. 5a the strain levels are tensile and relatively small, i.e., 0.02–0.005%, since the temperature difference between full and partial load is small. Sabau and Wright [23] found that differential thermal expansion (due to cycling of

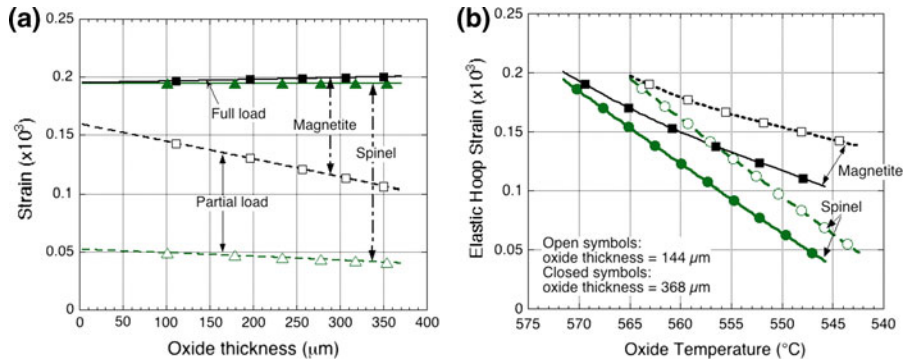


Fig. 5 Evolution of the average hoop strain for the elastic case (NG–NC): does not include OGI strain and creep phenomena **a** over four years of oxide growth, and **b** during the transition from full load to the partial load

the steam temperature between 460 and 550 °C) increased these strain levels, whereas the pressure drop associated with the full-partial load transition yielded a decrease in the strain levels. Thus, for the boiler conditions considered here, the pressure variation has a larger effect on the strain level in the oxides than does the temperature variation.

Case NG: Creep of the Alloy and Oxide Included, but OGI Phenomena Not Considered

When creep phenomena were not included, both spinel and magnetite layers were in tension (Fig. 5a) for both full load and partial load regimes. However, the inclusion of creep phenomena resulted in the magnetite and spinel being in compression for most part of the operating cycle at both full and partial load, as shown in Fig. 6a. For new (or clean) tubes at oxide thicknesses up to 50 μm, there was a sharp decrease in the oxide strains with increasing oxide thickness, followed by a slow increase. Thus, as expected intuitively, the general effect of creep was to decrease the value of the elastic strain in the oxides during both full and partial load regimes. In order to fully assess the applicability of each case, the *maximum* values for the

creep hoop strain, $\bar{\epsilon}_{\theta,cr}^{max} = \max \left[\int_{r=r_1, r_N} \epsilon_{\theta,cr}(r, \tau) dr \right]_{\tau=0, t}$, and the von Mises stress in the metal and oxide layers are shown in Table 11.

Cases Involving Dilatational Strains

The first case considered involving OGI strains used the traditional dilatational model (*DIL_ω*). Case *DIL₁* was not considered here as Bernstein [13] indicated that $\omega = 1$ was not appropriate for the dilatational formulation. Instead, following Bernstein [6], dilatational case *DIL_{0,1}* were considered (Table 10). Case *D–NOC* (creep of the alloy, but no oxide creep) was considered first since it is usually assumed that creep in the metal is more important than in the oxide [2]. However, as shown in Fig. 6b,

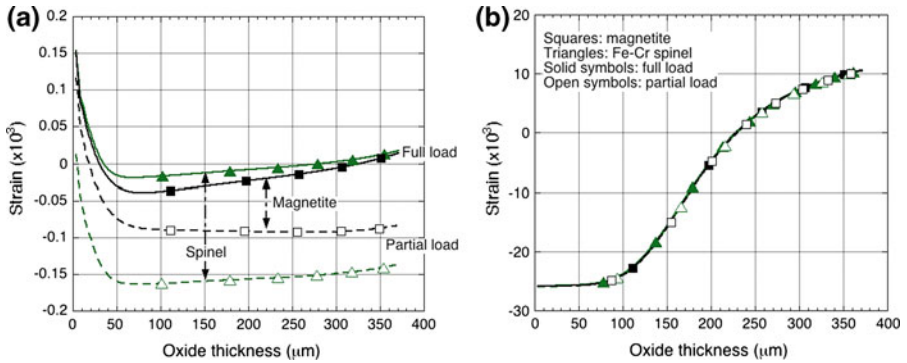


Fig. 6 Evolution of the average hoop strain for Cases **a** NG-C (creep phenomena included, but no OIG strain), and **b** DIL_{0.1}-NOC (DIL_{0.1} strain included, but with creep phenomena only in the metal)

Table 11 Assessment of cases considered based on maximum values for the creep strains, $\bar{\varepsilon}_{\theta,cr}^{max}$, and von Mises stresses

Case	$10^3 \max(\varepsilon_{\theta,cr})$			Von Mises (MPa)	
	Metal	Spinel	Magnetite	Metal	Oxide
NG-NC	–	–	–	43	20
NG	3.05	5.03	5.15	44	8
D-NOC	20.7	–	–	41	2,089
D	1.36	–24.1	–25	40	7
R1	1.98	–3.64	–17	40	5.5
R2	1.98	2.68	1.42	40	6.7
RL1	1.61	–16.3	–17.5	40	4.6–7
RL2	1.92	–1.1	–2.34	40	5
RL3	1.97	1.93	0.67	40	6.5

although the calculated elastic strains for thin oxides were compressive, becoming tensile at oxide thicknesses greater than approximately 230 μm , the values of these strains were unrealistically large. Also, the von Mises stress in the oxide layers reached 2,089 MPa, an unrealistically high value (Table 11).

Case D incorporated OGI strains (i.e., DIL_{0.1}) together with creep in both metal and oxide. The oxide strains were acceptably small, similar for both oxides, and always compressive; the highest strains occurred under partial load conditions (Fig. 7a). However, as summarized in Fig. 7b, the calculated hoop creep strains were unrealistically large, approximately –2.5%.

Cases Involving Uniaxial OGI Strains

Cases R1 and R2 used the RAD_{ω} formulation for OGI strains RAD_1 and $RAD_{0.1}$, respectively (Table 10). The calculated average hoop strains for these cases decreased rapidly as the oxide grew to 20 and 50 μm , respectively, and then leveled

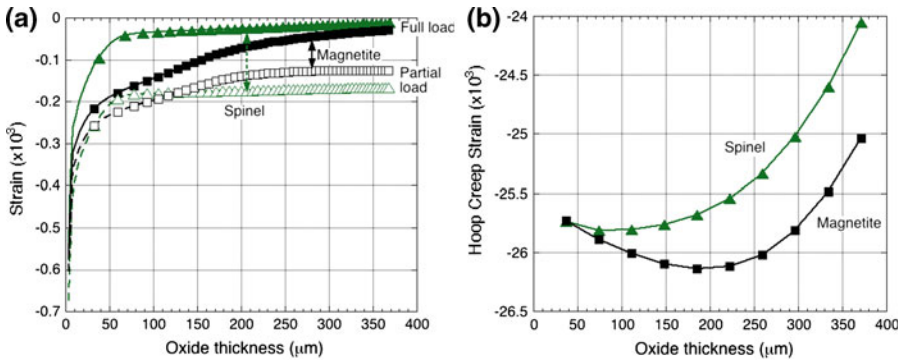


Fig. 7 Results for Case D, for inclusion of $\text{DIL}_{0.1}$ strain as well as creep phenomena in the oxide and metal, showing the evolution of **a** average elastic hoop strain, and **b** average hoop creep strain

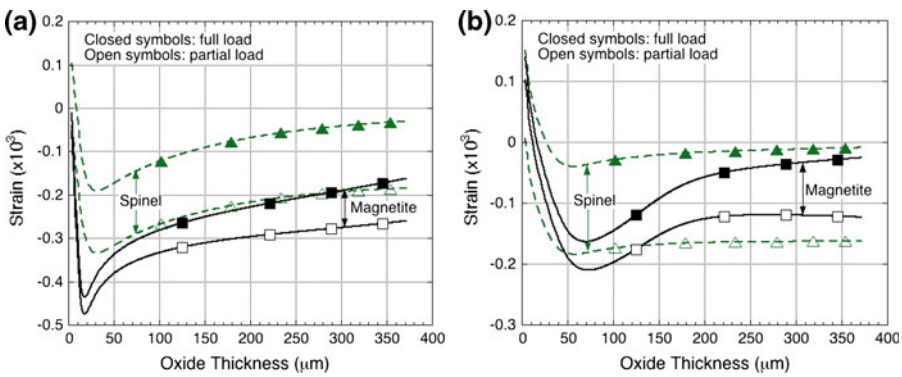


Fig. 8 Evolution of the average elastic hoop strain when uniaxial OGI strains (based on radial hoop strain formulations) are considered in addition to creep in the oxide and metal. **a** Case R1 (RAD_1) and **b** Case R2 ($\text{RAD}_{0.1}$)

off at negative values (Fig. 8). However, for Case R1 the *maximum* hoop creep strain ($\epsilon_{\theta,cr}$), which was computed in the magnetite layer at the end of the simulation (maximum time) was very large, approximately -1.7% (Table 11) while, for Case R2, the hoop creep strain had values of approximately $0.1\text{--}0.2\%$.

Cases Including Lateral Growth Effects

OGI strains based on the $\text{LAT}_B\text{RAD}_\omega$ formulations were considered next. The ω parameter was held constant at 0.1, since this value was found to yield acceptable results for the radial models. Three cases, RL1, RL2, and RL3 were conducted for three values of parameter B of 2×10^4 , 1×10^5 , and $5 \times 10^5 \mu\text{m}$, respectively. Figure 9 shows the evolution of the elastic hoop strains ($\epsilon_{\theta,ei}$) in the spinel and magnetite layers for these cases. The strain was found to decrease abruptly in the initial stages of oxide growth and then to increase asymptotically with increasing

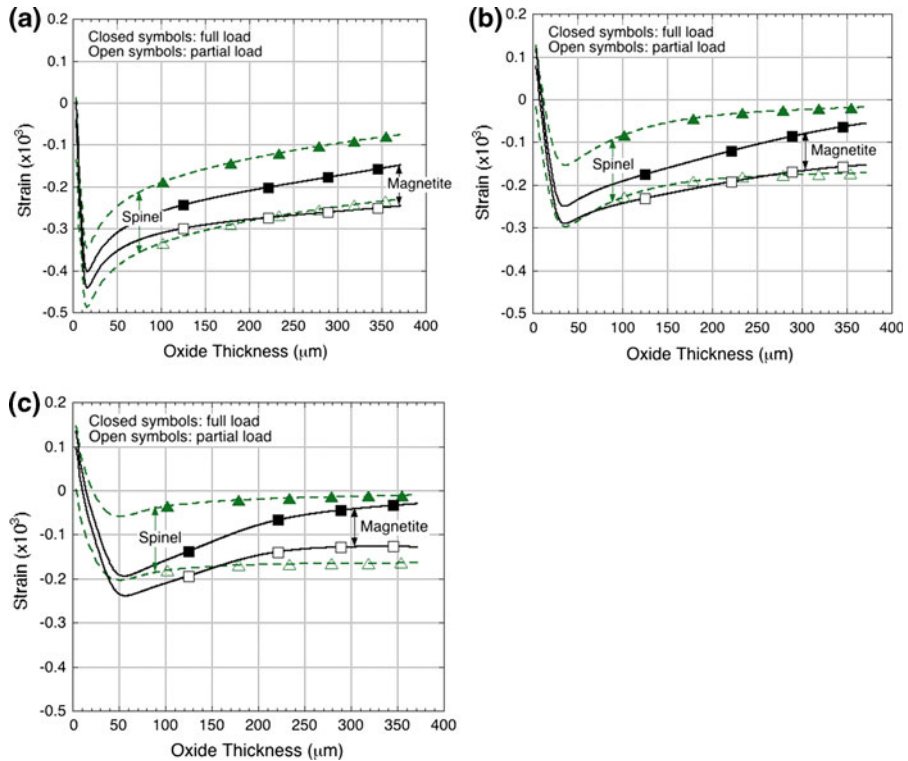


Fig. 9 The evolution of the average hoop strain, for Cases **a** RL1; **b** RL2; and **c** RL3

oxide thickness. For the three cases considered, the elastic hoop strains were always negative (compressive). Comparing the results for these RL cases suggests the following conclusions: (a) an initial stage of decreasing strains occurs over an oxide thickness that increases with the B factor, (b) the amount of strain decrease in the initial stages decreases as B increases, (c) the slope of the elastic hoop strain curve, at large oxide thicknesses, decreases as B increases.

The results for the creep strains for these cases are shown in Fig. 10. For Case RL1 (Fig. 10a), the hoop creep strain ($\varepsilon_{\theta,cr}$) in the magnetite layer reached unrealistically large (negative) values of approximately -1.75% for an oxide thicknesses of 370 μm . For Case RL2 the hoop creep strains in the oxide were always compressive and increased steadily with increasing oxide thickness to approximately 250–300 μm , at which point strain in the magnetite layer was approximately -0.25 , and -0.15% in the spinel layer. For Cases RL2 and RL3 the alloy experienced increasing tensile hoop creep strain with increasing oxide thickness to a value of approximately 0.2% at an oxide thickness of 370 μm . For Case RL3 the hoop creep strain eventually became positive for both oxide layers, with the highest strain in the spinel layer. As shown in Fig. 10b, at a scale thickness of 370 μm the creep hoop strain in the spinel layer was similar to that in the alloy (approx. $+0.2\%$), compared to $+0.07\%$ in the magnetite. It seems reasonable to

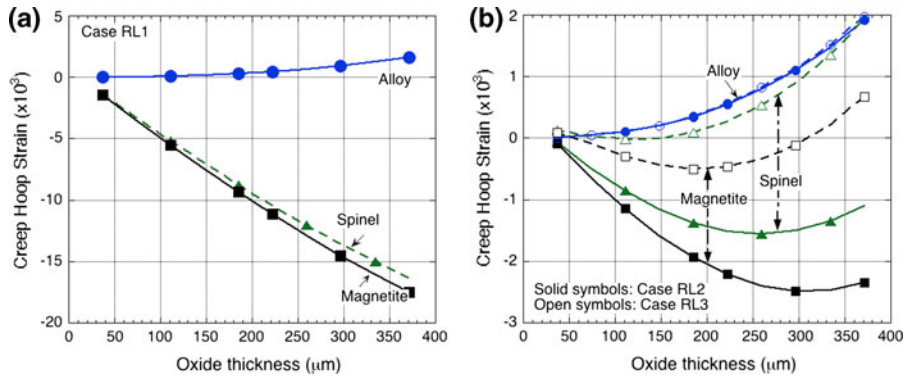


Fig. 10 Evolution of average **a** creep hoop strain for Case RL1, and **b** creep hoop strain for Cases RL2 and RL3

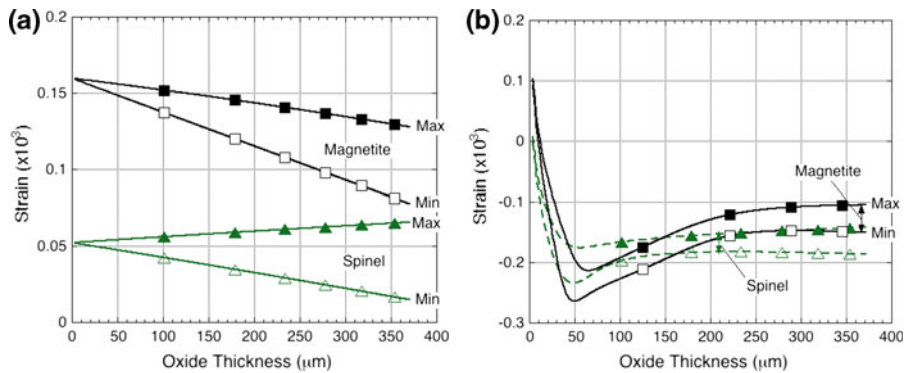


Fig. 11 Evolution of maximum and minimum elastic hoop strain in the oxide layers for Cases **a** NG–NC and **b** RL3

expect that the greater level of accommodation required in the spinel layer would result in ‘damage’ in the form of void formation or other microstructural changes.

Based on the results for the elastic strain, creep strains, and von Mises strain, it was concluded that Cases NG, R2, and RL3 produced acceptable results. Next, the maximum *spatial* values, i.e., $\epsilon_{\theta,el}^{r-max}(t) = \max[\epsilon_{\theta,el}(r,t)]_{r=r_1,r_N}$, and the corresponding minimum *spatial* values, i.e., $\epsilon_{\theta,el}^{r-min}(t) = \max[\epsilon_{\theta,el}(r,t)]_{r=r_1,r_N}$, were considered in order to assess the amount of variation within each oxide scale. The amount of strain variation in each oxide layer is virtually unknown, as most studies considered it to be negligible based solely on the fact that the oxide thickness is much smaller than that of the metal tube. Figure 11 shows the evolution of the minimum and maximum values of the *elastic* hoop strain for the NG–NC and RL3 cases. For Case NG–NC the range of the elastic hoop strain [i.e., $\max(\epsilon_{\theta,el}) - \min(\epsilon_{\theta,el})$] increased linearly with oxide thickness and, for the spinel, became

approximately of the same order of magnitude as the strain itself at oxide thicknesses larger than 200 μm (Fig. 11a). For Case RL3 the range of the elastic hoop strain was almost constant at approximately 0.005%, while the maximum strains were -0.01% and -0.015% in the magnetite ($>$ approx. 220 μm) and spinel ($>$ 130 μm) layers, respectively. Thus, the variation of the elastic hoop strain was not negligible, and must be taken into account when oxide strains are calculated.

Effects of Cooling to Room Temperature (Boiler Shut Down)

The evolution of the average elastic hoop strain during cooling to room temperature was considered in Cases NG, R2, and RL3. Cooling to room temperature was envisioned as a boiler shut-down event in which the steam pressure also decreases (see Table 8). In the absence of data on actual pressure variation with time for superheater boiler tubes (subcritical steam) during a shut down event, the pressure was assumed to decrease linearly to atmospheric pressure. The temperature at which the maximum strain was reached was determined by the thermal expansion properties of the alloy and each oxide layer. In contrast with the results obtained for the pure elastic case without OGI strain effects (NG–NC), for Cases NG, R2, and RL3 the average elastic hoop strain was found to reach a maximum at a temperature of approximately 400 $^{\circ}\text{C}$ for magnetite and 375 $^{\circ}\text{C}$ for the spinel layer (Fig. 12).

For Case NG–NC the evolution of the elastic hoop strain for a shut down event (Fig. 12a) and full-to-partial load transition (Fig. 5b) were found to be different since the variations in pressure and temperature were different in each case. At shut down the maximum strain attained in the magnetite was approximately twice than that for the spinel layer. Case NG–NC resulted in the largest value for strain among all the cases considered: the magnetite was at all times in tension, while the spinel layer switched from tension to compression at approximately 100 $^{\circ}\text{C}$. When creep was included (Case NG), the strain curves were moved to lower values overall, and the strain in the spinel layer became compressive for temperatures lower than 200 $^{\circ}\text{C}$ (Fig. 12b). As compared to the results for the NG–NC case, the maximum strain value for the magnetite layer was approximately 22% lower, and that for the spinel layer approximately 40% lower. The results for Cases R2 (Fig. 12c) and RL3 (12d) yielded slightly lower strain values than for Case NG, but the differences between R2 and RL3 were negligible. This could be due to the fact that the lateral OGI strains were very small.

Summary and Implications

This appears to be the first study to account for inelastic effects on the development of strain in steam-side oxides formed in boiler tubes that are subject to an actual operating schedule. For the temperature range considered (500–600 $^{\circ}\text{C}$, which was intended to match closely that encountered in boiler service) exploration of stress relaxation by creep indicated that the oxide layers experienced more creep than the alloy. In this study an eigenstrain approach was used to formulate oxidation strains in which the oxidation eigenstrains were prescribed. Several cases were considered

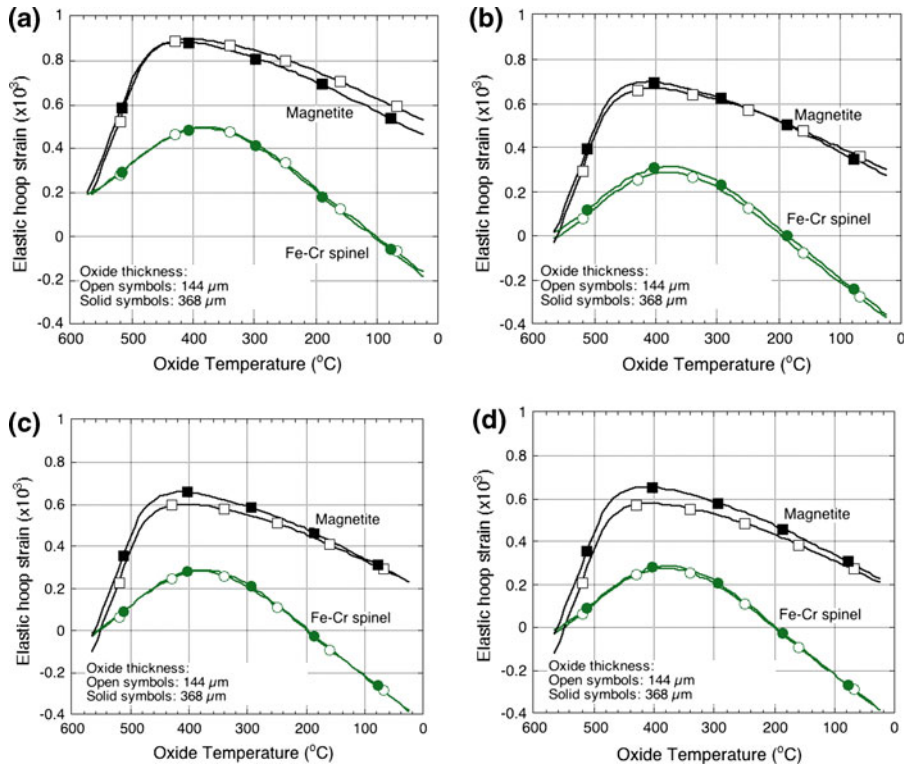


Fig. 12 Evolution of the average elastic hoop strain, $\epsilon_{\theta,el}$, within the spinel and magnetite layers during cooling from the oxide growth temperatures (T_{gr}) associated with full load conditions to room temperature, for two different oxide thicknesses, for Cases **a** NG–NC, **b** NG, **c** R2, and **d** RL3

for each formulation. For the dilational strain case, large von Mises stresses in the oxide layers could not be accommodated by creep in the oxide. It was found that the oxide growth-induced strain development is a necessary consideration, but that selection of the particular OGI strain model is a very important factor in determining the magnitude of the predicted oxide strains. Calculations for different scenarios showed that the incorporation of the OGI strains has a dramatic effect on the state of deformation in the oxide. The inclusion of creep considerations yielded a decrease in the level of elastic strains in the oxides, as expected intuitively.

Overall, when strain accumulation from oxide growth and relaxation from creep are considered, the net state of strain in an oxide growing on a tube subjected to routine boiler load cycling conditions appears to be eventually compressive with relatively low values. As shown in Fig. 11b (Case RL3), in the initial stages of oxide growth under load-following cycling conditions (but in the absence of a shut down) the magnetite layer develops a compressive strain, reaching a maximum of $>0.025\%$ at a total oxide thickness of approximately 50 μm , but that the compressive strain decreases gradually to a value between 0.01 and 0.15% with further thickening of the oxide. The strain evolution in the spinel layer follows a

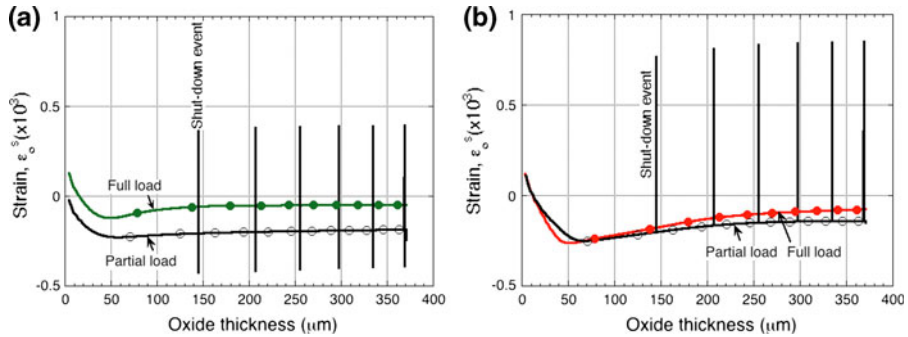


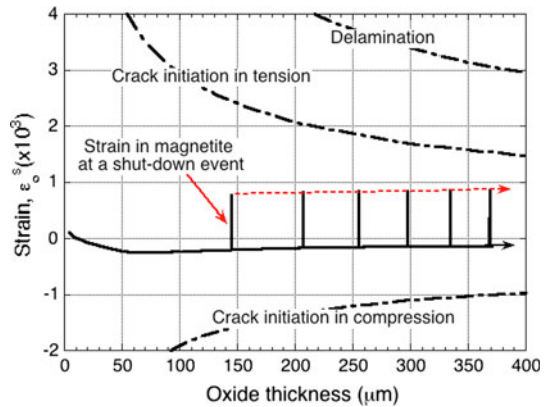
Fig. 13 Evolution of strain (ε_{θ}^s , strain that generates stress) as a function of total scale thickness for a boiler schedule that involves load cycling between maximum and partial load as well as periodic shut downs for **a** spinel layer; and **b** magnetite layer

similar path, reaching essentially steady state strain values between 0.015 and 0.19%. The imposition of conditions associated with a boiler shut down yields the development of strain differentials between the two oxide layers, as indicated in Fig. 12d.

The predicted maximum and minimum hoop strains that generate stress (ε_{θ}^s) for magnetite (obtained from the superimposition of shutdown events on the daily cycling schedule) are shown in Fig. 13a for the spinel layer, and Fig. 13b for the magnetite layer, assuming that a shutdown event occurs from the partial load condition. In this representation, the strains associated with the shutdown event appear as spikes; for the spinel layer the increase in tensile strain at the start of the shutdown event is replaced by a compressive strain of about equal magnitude at room temperature (c.f. Fig. 12d), whereas in the magnetite layer the maximum increase in tensile strain occurs on cooling through 400 °C, with a smaller residual tensile strain at room temperature. The maximum differential strain between the spinel and magnetite layers occurs at room temperature (approximately 0.06% from Case RL3, Fig. 12d). This differential strain would be expected to raise the potential for shear between the spinel and magnetite layers; if this were to be concentrated along the interface between these layers (by, for instance, the presence of flaws such as voids), separation could occur.

The potential for the application of this model as a predictive tool is illustrated simplistically in Fig. 14, which shows the ‘strain trajectory’ for the magnetite layer (from Fig. 13b) superimposed on an Armit et al.-style damage map of the critical strains for oxide failure [37, 38] based on fracture toughness concepts for elastic, brittle materials. On the assumption that these criteria for damage would be the same for elastic materials, intersection of the ‘strain trajectory’ with the damage criteria can be used to signal failure (for a single oxide layer). However, for Case RL3 the strain trajectories based on the maximum strains associated with shut down events do not predict scale failure within the range of oxide thicknesses considered whereas, in practice, scale spallation from alloy T22 has been observed at scale thicknesses less than 400 μm. However, as indicated above, relatively small changes in the values of OIG strain parameters used in this model can effect large

Fig. 14 Damage map showing critical strains and predicted maximum and minimum values of ε_0^s for the magnetite layer during shutdown events for Case RL3 (includes lateral growth strains and creep effects)



changes in the calculated strains. Further, the influence of flaws that develop in real oxide scales and can significantly influence the state of strain and stress has not yet been incorporated into the model. The recent advances on criteria for failure of actual scale structures are being summarized in Schütze et al. [39], but experimental results are needed to define the conditions for damage initiation, scale failure, and spallation under well controlled conditions in order to assess the validity of the inelastic models such as that presented here. Future work should include a methodology to obtain oxide growth-induced parameters based on experimental evidence and/or theoretical diffusion models, and provide some quantification of the evolution of flaws (size, shape, location) in real scales, together with their effects on the state of strain and stress.

Conclusions

In this study, approaches for evaluating inelastic effects resulting from creep and from volume change due to oxide growth on the processes leading to the spallation of oxides grown in steam on alloy T22 (Fe-2.25Cr-1Mo, wt%) were evaluated. Several formulations for the oxide growth-induced phenomena were critically examined, and the nature of available approaches for quantifying oxide growth-induced strain was considered to be contentious. Nevertheless, the solution algorithm used to represent oxide growth-induced strain (in the absence of creep phenomena) was validated for the radial model against published data. As noted by others, the level of strain in the oxide layers was found to depend strongly on the formulation used for the oxide growth-induced strain model, and the values of strain in the magnetite and spinel layers were found to be different. Using values of the relevant parameters (including time) consistent with an oxide grown on the inside of a steam tube subjected to the varying conditions of boiler operation, strain evolution during cyclic operation and during shut down events was investigated. It was found that, during cooling from full load to room temperature, higher levels of strain were developed in the magnetite than in the spinel layer; the oxide strain was maximum at a temperature of approximately 400 °C for magnetite and 375 °C for the spinel layer.

Acknowledgements This research was sponsored by the Electric Power Research Institute under a Work for Others program (agreement No. EP-P18842/C9306) with the U.S. Department of Energy, Office of Fossil Energy (DOE-FE). The authors would like to thank John Shingledecker of EPRI for guidance on the use of creep data and insightful discussions. Also, we would like to thank Dr. Bruce Pint and Dr. Thomas Wakins at ORNL for reviewing the manuscript. This submission was sponsored by a contractor of the United States Government under contract DE-AC05-00OR22725 with the United States Department of Energy. The United States Government retains, and the publisher, by accepting this submission for publication, acknowledges that the United States Government retains, a nonexclusive, paid-up, irrevocable, worldwide license to publish or reproduce the published form of this submission, or allow others to do so, for United States Government purposes.

Appendix 1

Solution for the Stress–Strain Equations for a Plane-Strain Approximation in Axi-Symmetrical Geometry

The solution developed in this study for the thermal stresses in cylindrical coordinates extended that presented by Noda et al. [40] to a temperature- and spatial-dependent thermal strain. The equations for the displacement and stresses in the i -th layer and j -th position are:

$$u_{i,j}(r_j, T_{R,i,j}, T_{i,j}) = c_i r_j + \frac{d_i}{r_j} + \frac{1 + \nu_i^*}{r_j} I_i(r_j, T_{R,i,j}, T_{i,j}) + 0.5(u_{i,j}^{ox} + u_{i,j}^{cr})$$

$$u_{i,j}^{ox} = (1 - \nu_i^*) (\varepsilon_{r,ox} - \varepsilon_{\theta,ox}) r_j \ln(r_j) \tag{12}$$

$$u_{i,j}^{cr} = \frac{1 + \nu_i^*}{r_j} J_i(r_j, \varepsilon_{s,cr}) + (1 - \nu_i^*) r_j J_i(r_j, \varepsilon_{d,cr})$$

$$\varepsilon_{r,i,j} = \frac{\partial u_{i,j}}{\partial r} \tag{13}$$

$$\frac{\sigma_{r,i,j}}{E_i^*} = \frac{c_i + \nu_i \varepsilon_o - \varepsilon_{r,i,j}^{ox}}{1 - \nu_i^*} - \left(\frac{d_i}{1 + \nu_i^*} + I_i(r_j, T_R, T_{i,j}) \right) \frac{1}{r_j^2} - \varepsilon_{r,i,j}^{cr}$$

$$\varepsilon_{r,i,j}^{ox} = \nu_i \varepsilon_{ox,z} + 0.5 (\varepsilon_{ox,r} + \varepsilon_{ox,\theta}) - 0.5 (1 - \nu_i^*) (\varepsilon_{ox,r} - \varepsilon_{ox,\theta}) \ln(r_j) \tag{14}$$

$$\varepsilon_{r,i,j}^{cr} = 0.5 \frac{J_i(r_j, \varepsilon_{s,cr})}{r_j^2} - 0.5 J_i(r_j, \varepsilon_{d,cr})$$

$$\frac{\sigma_{\theta,i,j}}{E_i^*} = \frac{c_i + \nu_i \varepsilon_o - \varepsilon_{\theta,i,j}^{ox}}{1 - \nu_i^*} - (1 + \nu_i) \varepsilon_{th,i}(T_R, T_{i,j}) + \left(\frac{d_i}{1 + \nu_i^*} + I_i(r_j, T_R, T_{i,j}) \right) \frac{1}{r_j^2} - \varepsilon_{\theta,i,j}^{cr}$$

$$\varepsilon_{\theta,i,j}^{ox} = \nu_i \varepsilon_{ox,z} + 0.5 (\varepsilon_{ox,r} + \varepsilon_{ox,\theta}) - 0.5 (1 - \nu_i^*) (\varepsilon_{ox,r} - \varepsilon_{ox,\theta}) [1 + \ln(r_j)]$$

$$\varepsilon_{\theta,i,j}^{cr} = \varepsilon_{\theta,cr} + \nu_i \varepsilon_{z,cr} - 0.5 \frac{J_i(r_j, \varepsilon_{s,cr})}{r_j^2} - 0.5 J_i(r_j, \varepsilon_{d,cr}) \tag{15}$$

$$\sigma_{z,i,j} = \nu_i (\sigma_{r,i,j} + \sigma_{\theta,i,j}) + E_i (\varepsilon_o - \varepsilon_{th,i}(T_R, T_{i,j}) - \varepsilon_{ox,z} - \varepsilon_{cr,z}) \tag{16}$$

where j varies between 1 and M_i . $I_i(r_j, T_1, T_2) = (1 + \nu_i) \int_{rb_{i+1}}^{r_j} \varepsilon_{th,i}(T_1, T_2) r dr$,
 $J_i(r_j, \varepsilon) = \int_{rb_{i+1}}^{r_j} \varepsilon dr$, $\varepsilon_{d,cr} = \frac{\varepsilon_{r,cr} - \varepsilon_{\theta,cr}}{r}$, and $\varepsilon_{s,cr} = (\varepsilon_{r,cr} + \varepsilon_{\theta,cr} + 2\nu\varepsilon_{z,cr})r$.

The constant ε_o and coefficients c_i and d_i were determined using equations for the continuity of radial stresses, $\sigma_{r,i,M_i} = \sigma_{r,i+1,1}$, and displacements in the radial direction at boundary radii between adjacent layers, $u_{i+1,1} - u_{i,M_i} = \Delta u_i$. For growth of oxide at internal interfaces $\Delta u_i = 0$. For oxide growth at the oxide–steam surface Δu_i may have to be obtained based on oxide growth-induced strain and mass transport of species to the surface location where the oxide grows. In the absence of details of the transporting species, $\Delta u_i = 0$ for growth of oxide at the surface. The pressure condition on the hot gas side and steam side is given by:

$$\sigma_{r,1,1} = -P_g, \text{ and } \sigma_{r,N,M_N} = -P_{st} \tag{17}$$

where P_g and P_{st} are the pressures of the flue gas and steam, respectively. The axial force equation used to solve for model constants was considered only for the GPS assumption, i.e., when ε_o was not set, but needed to be evaluated. When the axial load was known, the condition for a zero axial force was written as:

$$2\pi \int_{rb_{N+1}}^{rb_1} \sigma_z r dr = F_z \tag{18}$$

Appendix 2

Creep Model

The creep strains for direction k (i.e., r , θ , and z) at a given time (t) are obtained by accumulation of creep strain increments within the current time increment (Δt):

$$\begin{aligned} \varepsilon_{k,cr}(t + \Delta t) &= \varepsilon_{k,cr}(t) + \Delta \varepsilon_{k,cr} \\ \Delta \varepsilon_{k,cr} &= 1.5 \frac{\sigma_k - p}{\sigma_{eq}} \Delta \varepsilon_{eq,cr} \\ \Delta \varepsilon_{eq,cr} &= \Delta t \dot{\varepsilon}_{cr}(\sigma_{eq}, T) \end{aligned} \tag{19}$$

where $p = (\sigma_r + \sigma_\theta + \sigma_z)/3$ is the pressure, and σ_{eq} is the von Mises equivalent stress, given as,

$$\sigma_{eq} = \sqrt{(\sigma_r - \sigma_\theta)^2 + (\sigma_\theta - \sigma_z)^2 + (\sigma_r - \sigma_z)^2} / \sqrt{2}.$$

References

1. I. G. Wright, A. S. Sabau, and R. B. Dooley, *Materials Science Forum* **595–598**, 387 (2008).
2. H. Steiner, J. Konys, and M. Heck, *Oxidation of Metals* **66**, 37 (2006).

3. B. Panicaud, J. L. Grosseau-Poussard, and J. F. Dinhut, *Applied Surface Science* **252**, 5700 (2006).
4. B. Panicaud, J. L. Grosseau-Poussard, and J. F. Dinhut, *Journal of Neutron Research* **12**, 27 (2004).
5. B. Panicaud, J. L. Grosseau-Poussard, P. O. Renault, J. F. Dinhut, D. Thiaudière, and M. Gailhanou, *Journal of Neutron Research* **12**, 57 (2004).
6. F. H. Stott, *Reports on Progress in Physics* **50**, 861 (1987).
7. F. N. Rhines and J. S. Wolf, *Metallurgical and Materials Transactions* **1**, 1701 (1970).
8. A. G. Evans, G. B. Crumley, and R. E. Demaray, *Oxidation Metals* **20**, 193 (1983).
9. V. K. Tolpygo, J. Dryden, and D. R. Clarke, *Acta Materialia* **46**, 927 (1998).
10. D. R. Clarke, *Acta Materialia* **51**, 1393 (2003).
11. C. H. Hsueh and A. G. Evans, *Journal of Applied Physics* **54**, 6672 (1983).
12. N. B. Pilling and R. E. Bedworth, *Journal of the Institute of Metals* **29**, 529 (1923).
13. H. L. Bernstein, *Metallurgical and Materials Transactions A* **18**, 975 (1987).
14. M. Schütze, *Protective Oxide Scales and their Breakdown* (John Wiley, Chichester, 1997).
15. A. G. Evans and R. M. Cannon, *Materials Science Forum* **43**, 243 (1989).
16. A. M. Limarga, D. S. Wilkinson, and G. C. Weatherly, *Scripta Materialia* **50**, 1475.
17. D. R. Clarke, *Solid State and Materials Science* **6**, 237 (2002).
18. B. Panicaud, J. L. Grosseau-Poussard, and J. F. Dinhut, *Computational Materials Science* **42**, 286 (2008).
19. B. Panicaud, J. L. Grosseau-Poussard, J. F. Dinhut, and D. Thiaudière, *Applied Surface Science* **252**, 8414 (2006).
20. E.-S. Oh, J. R. Walton, D. C. Lagoudas, and J. C. Slattery, *Acta Mechanica* **181**, 231 (2006).
21. R. K. Penny and D. L. Marriott, *Design for Creep* (Chapman & Hall, London, 1995).
22. M. McLean and B. F. Dyson, *Journal of Engineering Materials and Technology-Trans ASME* **122**, 273 (2000).
23. A. S. Sabau and I. G. Wright, *Journal of Applied Physics* **106** (2009).
24. H. J. Frost and M. F. Ashby, *Deformation-Mechanism Maps* (Pergamon Press, Oxford, 1982), p. 62.
25. B. J. Cane, *International Journal of Pressure Vessels and Piping* **10**, 11 (1982).
26. J. Shi and T. Endo, *Tetsu-to- agane* **80**, 795 (1994).
27. M. W. D. van der Burg, E. van der Giessen, and R. C. Brouwer, *Acta Materialia* **44**, 505 (1996).
28. P. Mayer and A. V. Manolescu, in *High-Temperature Corrosion*, ed. R. A. Rapp, International Corrosion Conference Series NACE-6 (NACE, Houston, Texas, 1983), p. 368.
29. A. G. Crouch and J. Robertson, *Acta Metallurgica et Materialia* **38**, 2567 (1990).
30. I. G. Wright, P. F. Tortorelli, and M. Schütze, EPRI Report No. 1013666 (2007).
31. R. J. Brown, in *Techniques for Multiaxial Creep Testing*, eds. D. I. Gooch and I. M. How (Elsevier Applied Science, London, 1985), p. 311.
32. K. Zarrabi and L. Ng, *Journal of Pressure Vessel Technology*, **130**, 041201 (2008).
33. M. Pronobis, W. Wojnar, and J. Czepelak, *Forschung im Ingenieurwesen* **69**, 29 (2004).
34. L. Xu, J. A. Khan, and Z. Chen, *Applied Thermal Engineering* **20**, 545 (2000).
35. I. Benyó, J. Kovács, J. Mononen, and U. Kortela, in *Proceedings of 16th European Simulation Symposium (ESS2004)* (Budapest, Hungary, 2004), p. 120.
36. M. M. P. Gonzalez, F. J. F. Garcia, I. S. Ramon, and H. S. Roces, *Energy* **31**, 665 (2006).
37. J. Armitt, D. R. Holmes, M. I. Manning, D. B. Meadowcroft, and E. Metcalfe, EPRI Report No. FP 686 (1978).
38. M. Schütze, *Materials at High Temperatures* **22**, 147 (2005).
39. M. Schütze, P. F. Tortorelli, and I. G. Wright, Submitted for publication to the *Materials at High Temperatures*, July 2009.
40. N. Noda, R. B. Hetnarski, and Y. Tanigawa, *Thermal Stresses*, 2nd edn (Taylor and Francis, New York, 2003).